JGR Solid Earth

RESEARCH ARTICLE
10.1029/2023JB028409

Special Collection:
Advances in understanding volcanic processes

Physics-Based Forecasts of Eruptive Vent Locations at Calderas

L. Mantiloni[1,2,3], E. Rivalta[1,4], K. R. Anderson[5], T. Davis[6], and L. Passarelli[7]

[1]Section 2.1 'Physics of Earthquakes and Volcanoes', GFZ German Research Centre for Geosciences, Potsdam, Germany, [2]Institute of Geosciences, University of Potsdam, Potsdam, Germany, [3]Department of Earth and Environmental Sciences, University of Exeter, Penryn, United Kingdom, [4]Department of Physics and Astronomy, Alma Mater Studiorum University of Bologna, Bologna, Italy, [5]U.S. Geological Survey, Moffett Field, CA, USA, [6]Department of Earth Sciences, University of Oxford, Oxford, UK, [7]INGV Istituto Nazionale di Geofisica e Vulcanologia, Sezione di Bologna, Bologna, Italy

Abstract Constraining stresses in the Earth's crust in volcanic regions is critical for understanding many mechanical processes related to eruptive activity. Dike pathways, in particular, are shaped by the orientation of principal stress axes. Therefore, accurate models of dike trajectories and future vent locations rely on accurate estimates of stresses in the subsurface. This work presents a framework for probabilistic constraint of the stress state of calderas by combining three-dimensional physics-based dike pathway models with observed past vent locations using a Monte Carlo approach. The retrieved stress state is then used to produce probability maps of future vent opening across a caldera. We test our stress inversion and vent forecast approach on synthetic scenarios, and find it successful depending on the distribution of the available vents and the complexity of the volcano's structural history. We explore the potential and limitations of the approach, show how its performance is sensitive to the assumptions in the models and available prior information, and discuss how it may be applied to real calderas.

Plain Language Summary Many processes at volcanoes are influenced by the stress state in the subsurface, which results from various forces, such as the gravitational loading due to redistribution of mass following the formation of topographic features. In particular, magma often opens its own pathway from a magma chamber to the surface along trajectories that are sensitive to the distribution of stress within the rocks. Therefore, knowledge of the stress state in volcanoes is critical to understand, and possibly forecast, magma pathways and the locations where they may reach the surface. In this work, we develop a framework to constrain the stress state at calderas. We estimate the stress field so that it is consistent with pathways that link the magma chamber with the eruptive vents of past eruptions. Then, we employ the estimated stress state to simulate future magma pathways and study the expected distribution of the resulting eruptive vents across the caldera, identifying the areas which are more likely to host future eruptions. We test our approach on artificially generated scenarios and explore the potential, limitations, and possible future applications of our work.

Key Points:

- We use past vent locations and a Bayesian framework to constrain the stress state at calderas with a physics-based model of dike pathways
- We exploit the posterior information on stress state at calderas to produce probability maps of future vent opening locations
- We test the stress inversion and vent forecast on synthetic calderas, exploring the potential and limitations of the strategy

Supporting Information:

Supporting Information may be found in the online version of this article.

Correspondence to:

L. Mantiloni,
l.mantiloni@exeter.ac.uk

Citation:

Mantiloni, L., Rivalta, E., Anderson, K. R., Davis, T., & Passarelli, L. (2024). Physics-based forecasts of eruptive vent locations at calderas. *Journal of Geophysical Research: Solid Earth*, *129*, e2023JB028409. https://doi.org/10.1029/2023JB028409

Received 29 NOV 2023
Accepted 7 AUG 2024

Author Contributions:

Conceptualization: L. Mantiloni, E. Rivalta, K. R. Anderson, T. Davis, L. Passarelli
Formal analysis: L. Mantiloni, E. Rivalta, K. R. Anderson, T. Davis, L. Passarelli
Funding acquisition: E. Rivalta
Investigation: L. Mantiloni, E. Rivalta, K. R. Anderson, T. Davis, L. Passarelli
Methodology: L. Mantiloni, E. Rivalta, T. Davis
Project administration: E. Rivalta
Resources: E. Rivalta

1. Introduction

Volcanoes host a wide range of mechanical processes modulated by stress, such as seismicity and the emplacement of magma. The stress in the subsurface of volcanic systems results from the interplay of several mechanisms, such as the gravitational loading due to the effects of previous eruptions (e.g., progressive accumulation of erupted material, McGuire & Pullen, 1989; Roman & Jaupart, 2014; Walter et al., 2005), pressurization of a magma reservoir (O. H. Muller & Pollard, 1977; Pansino & Taisne, 2019), seismicity (Hill et al., 2002; Seropian et al., 2021), hydrothermal activity (Currenti et al., 2017; Fournier & Chardot, 2012; Rinaldi et al., 2010), or viscoelastic relaxation in heated rocks (Del Negro et al., 2009; Head et al., 2019). Among the numerous stress-driven and stress-modifying processes, magmatic dikes are especially important. As widely discussed and suggested by empirical evidence (Anderson, 1937; O. H. Muller & Pollard, 1977; Pollard, 1987; Gudmundsson, 1995), dike pathways and dike-fed fissures orient roughly perpendicular to the direction of the least compressive stress axis. Thus, modeling the stress state of a volcano with a sufficient spatial resolution might hold the key to forecast where a dike will breach the surface. Moreover, the importance of stress models reaches beyond volcanic hazard assessment, as geothermal exploration (e.g., Cloetingh et al., 2010), hydraulic fracturing (e.g., Busetti & Reches, 2014) and planning of underground facilities (e.g., Jo et al., 2019) all rely on estimates of the local stress field.

Software: L. Mantiloni
Supervision: E. Rivalta
Validation: L. Mantiloni, E. Rivalta
Visualization: L. Mantiloni
Writing – original draft: L. Mantiloni, E. Rivalta
Writing – review & editing: K. R. Anderson, T. Davis, L. Passarelli

Recently, new strategies to quantify the state of stress of volcanoes have been proposed. Rivalta et al. (2019) calibrated a model of the stress state in Campi Flegrei caldera, Italy, so that the resulting dike trajectories connected the inferred magma chamber with the locations of past vents. To do so, they combined a physics-based model of dike pathways in two dimensions (2D), in which dikes orient perpendicular to the direction of the least compressive stress axis, with a stress field determined by caldera unloading and tectonic extension and a Monte Carlo approach to estimate the relative magnitude of those stresses. Mantiloni et al. (2021) tested a similar strategy with analog models involving air-filled cracks propagating in stressed gelatin blocks. They used a subset of the observed trajectories to constrain the stress state within the gelatin; the inferred stresses were then used to forecast the arrivals of the remaining observed trajectories.

Maerten et al. (2022) constrained tectonic stress and magma chamber overpressure by matching modeled orientations of principal stresses with exposed dikes or past eruptive fissures. Zhan et al. (2022) reproduced the observed rotation of fault plane solutions during an unrest episode at Augustine Volcano, Alaska, using a trial-and-error optimization of three-dimensional (3D) stress models comprising tectonic stress, gravitational loading due to the volcanic edifice and an inflating, static dike.

Of these studies, only Rivalta et al. (2019) and Mantiloni et al. (2021) used the inferred stresses to forecast the locations of future eruptions, testing the forecasts with a subset of the observations. These studies show the potential of physics-based vent forecasting as an alternative to well-established data-driven approaches (Bevilacqua et al., 2015; Connor & Hill, 1995; Selva et al., 2012).

In order to apply such approaches to real volcanoes, fully 3D models are required. Three-dimensional dike trajectory models have been recently developed by Sigmundsson et al. (2015); Davis et al. (2020, 2021) and Mantiloni et al. (2023a). In particular, Davis et al. (2020, 2021) simulated the evolving shape of a stress-driven dike, while Mantiloni et al. (2023a) developed a propagation model for a penny-shaped dike of fixed radius, which can be considered as a 3D extension of the popular 2D models in which dike trajectories are determined from the principal stress axes. Complementing 3D dike trajectory models, 3D stress models have been available for decades (e.g., McGuire & Pullen, 1989; McTigue & Mei, 1987). However, constraining the stress state of volcanic systems is still an open problem. Specifically, assessing the relative importance of the different stress contributions is still challenging.

In this study, we develop a stress inversion method in 3D that accounts for gravitational loading due to realistic topographies and allows us to forecast the future locations of vents. We test our strategy on synthetic scenarios, so that we can explore the performance and drawbacks of the strategy on known settings.

2. Methods

2.1. The Inverse Problem of Stress at Volcanoes

We consider the problem of determining the elastic stresses that drove magma-filled dikes from a magma reservoir of roughly known location and geometry to a set of surface vents (Figure 1a).

We detail here some general assumptions. First, vent locations in nature are known with some uncertainty, as the early eruptive fissure geometry may be hidden by eruptive structures, such as spatter cones (Muirhead et al., 2016; Reches & Fink, 1988). Here, however, we take vent locations as points that are known exactly, each produced by a different dike. We assume that dikes originate from a "dike nucleation zone" at depth, defined as a volume where magma is present and dike nucleation is promoted, for instance due to stress concentration (e.g., Chestler & Grosfils, 2013; Grosfils, 2007; Gudmundsson, 2006). Identifying the dike nucleation zone amounts to gathering information on the location, size, and shape of a magma reservoir through analysis of independent observations, such as inversion of ground deformation data, seismic tomography, magnetotelluric and resistivity imaging, or petrological information, and making sensible assumptions on probable dike nucleation locations within or around the reservoir. If the above information were exactly known, D would narrow down to a set of N points in the subsurface. In a realistic case, however, identifying the dike nucleation zone involves several uncertainties. We account for such uncertainties by describing D in terms of a probability density function (PDF).

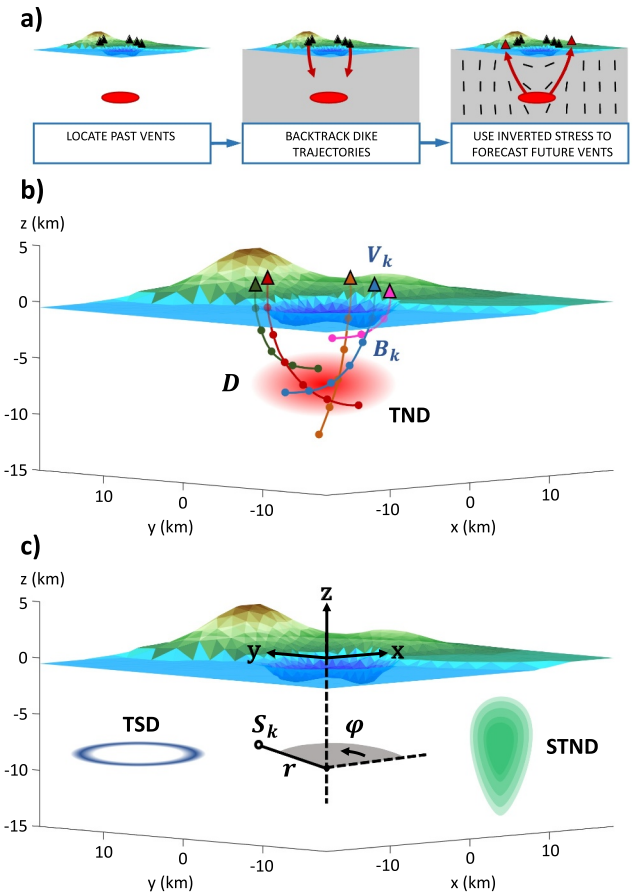

Figure 1. (a) Stress inversion and vent forecast strategy: starting from distribution of past vents (black triangles) and prior information on the magma reservoir (red ellipse), we constrain the stress field so that backtracked dike trajectories, B_k (red curves), are consistent with both; then, forecast future dike trajectories and vents (red triangles). (b) Inverse problem: eruptive vents (triangles) with locations V_k, and respective B_k (colored curves), crossing the dike nucleation zone, D. D is described by the probability density function p, here a trivariate normal distribution (TND, shaded red volume). Dots along B_k: steps of trajectory calculations (see Section 2.2). B_k stop after becoming horizontal or exceeding a 10-km depth threshold. (c) Cartesian reference frame, with origin at the caldera center, and coordinates r, ϕ of the cylindrical reference frame with same origin. The other two types of p used in this work are shown: the torus-shaped distribution (TSD) in blue, and the skewed, trivariate normal distribution (STND) in green. The types of p shown here are described in Section 3.1.

The stress model should account for the dominant stress-generating factors while limiting the number of parameters (herein termed stress parameters), which constitute the unknown quantities we aim to constrain. We also require a model of stress-driven dike trajectories with a limited number of parameters (dike parameters). Finally, we need a statistical procedure that samples the parameters. In the following, we outline the formal framework of our approach. We collect all symbols and abbreviations in Table 1.

2.1.1. Forward and Inverse Problem Formulation

Consider the setting of Figure 1b, described in a Cartesian reference frame where the z-axis is positive upward. We observe N vents, V_k, $k = 1, \ldots, N$, across a volcanic area. We describe the dike nucleation zone, D, in terms of a PDF $p(x, y, z)$ such that the probability of dike nucleation in a volume Ω in the crust is

$$\int_{\Omega} p(x, y, z)\, dV \tag{1}$$

where $dV = dx\, dy\, dz$.

We assume the crust is homogeneous, isotropic and linearly elastic, with density ρ_r, Young's modulus E and Poisson's ratio ν. Dike pathways from D to V_k are controlled by the stress field, which is described by a stress tensor $\sigma_{ij}(x, y, z)$. Tensional stresses are positive. We refer to the magnitudes of principal stresses, from most compressive to least compressive, as σ_1, σ_2, σ_3, and to the principal stress eigenvectors as $\vec{v}_1$, $\vec{v}_2$, $\vec{v}_3$, respectively.

We consider a model of dike trajectories, f, controlled by q stress parameters $\left(\theta_1, \ldots, \theta_q \equiv \vec{\theta}\right)$ that describe the volcano's state of stress (Section 2.3), and m dike and rock parameters $\left(\zeta_1, \ldots, \zeta_m \equiv \vec{\zeta}\right)$, describing, for example, the dike's size or the magma density (Section 2.2). f takes a nucleation point, $S_k \in D$, and calculates a dike trajectory, F_k, that links S_k to the vent location V_k unambiguously:

$$F_k = f\left(\vec{\theta}, \vec{\zeta}, S_k\right) : S_k \in D \rightarrow V_k, \quad k = 1, \ldots, N \tag{2}$$

Equation 2 describes the direct problem of dike pathway calculations. We describe $S_k \equiv \left(r_k^S, \phi_k^S, z_k^S\right)$ with the cylindrical reference frame in Figure 1c, where $r = \sqrt{x^2 + y^2}$ and ϕ is the angle measured on the xy plane counter-clockwise from the positive x-axis.

We formulate the "backward trajectory" problem as:

$$B_k = f_B\left(\vec{\theta}, \vec{\zeta}^B, V_k\right) : V_k \rightarrow S_k \in D, \quad k = 1, \ldots, N \tag{3}$$

that is, the model f_B recovers the trajectory of a dike that propagated upward and ended at vent V_k. We refer to the recovered trajectories as "backtracked" trajectories, B_k, as they are calculated from the vents downward. We stop the simulations at point B_k^{end} once the B_k stops descending or, alternatively, reaches a pre-established threshold in r or z (Figure 1b). If the backtracking model is accurate, B_k overlaps with F_k.

Table 1
Abbreviations, Symbols and Parameters

Description	Symbol	Units
General framework		
Coordinates (Cartesian)	x, y, z	m
Coordinates (cylindrical)	r, ϕ, z	m, rad, m
Vent locations	$V_k(x, y, z)$	
Number of vents	N	
Dike starting points	$S_k\left(r_k^S, \phi_k^S, z_k^S\right)$	
Dike nucleation zone	D	
PDF describing D	$p(x, y, z)$	
Stress parameters vector	$\vec{\theta}$	
Dike parameters vector (forward/backward)	$\vec{\zeta}/\vec{\zeta}^B$	
Trivariate normal distribution	TND	
Torus-shaped distribution	TSD	
Skewed trivariate normal distribution	STND	
Dike parameters ($\vec{\zeta}/\vec{\zeta}^B$)		
Magma density	ρ_m	kg/m^3
Forward/backtracked dike trajectories	F_k/B_k	
Stopping point of B_k	B_k^{end}	
Dike radius (penny-shaped crack)	c	m
Backtracked dike radius	c_B	m
Host rock properties and stress field		
Host rock density	ρ_r	kg/m^3
Mode I stress intensity factor	K	Pa$\sqrt{\text{m}}$
Fracture toughness	K_c	Pa$\sqrt{\text{m}}$
Young's modulus	E	Pa
Poisson's ratio	ν	
Stress tensor	$\sigma_{ij}(x, y, z)$	Pa
Principal stress axes	$\vec{v}_1, \vec{v}_2, \vec{v}_3$	
Principal stress magnitudes	$\sigma_1, \sigma_2, \sigma_3$	Pa
Stress parameters		
Caldera depth	d	m
Resurgent dome height	h	m
Tectonic stress tensor	σ_{ij}^T	Pa
MCMC, p parameters and vent forecast		
Data vector	$\vec{o}$	
Model vector	$\vec{m}$	
Number of MCMC iterations	M	
Proposal distribution	Q	
Q covariance matrix	Σ_Q	
Likelihood function	P	
p mean vector	$\vec{\mu}$	m
p covariance matrix	Σ	m^2

B_k intersects regions of different dike nucleation probabilities, depending on the stress and dike model parameters. The inverse problem amounts to constraining the parameters so that all the B_k cross volumes with highest nucleation probability.

2.1.2. Stress Inversion Approach

Following Bayes' Theorem (e.g., Gelman et al., 2013), we calculate the posterior PDF of the model parameters as:

$$\mathrm{P}(\vec{m}|\vec{o}) \propto \mathrm{P}(\vec{o}|\vec{m})\,\mathrm{P}(\vec{m}) \tag{4}$$

where $\vec{m}$ and $\vec{o}$ are the model and data vectors, respectively, $\mathrm{P}(\vec{o}|\vec{m})$ is the likelihood function, and $\mathrm{P}(\vec{m})$ is the prior information on the model parameters.

The data vector, $\vec{o}$, consists of a set of dike nucleation points, S:

$$\vec{o} = [S] \tag{5}$$

and the data space is the space of all possible dike nucleation points. The points S are only known through the PDF p, which represents the mode and variance of their locations and, thus, the state of information on the data (see, e.g., Tarantola, 2005). p is described by its own set of parameters, not included here for brevity, but detailed in Section 3.1.

In general, $\vec{m}$ includes both the stress ($\vec{\theta}$) and dike ($\vec{\zeta}^B$) parameters. Here, we fix the dike parameters, together with the host rock properties, so that the model vector only consists of the stress parameters, that is, $\vec{m} = \vec{\theta}$.

We now define the likelihood function, $\mathrm{P}(\vec{o}|\vec{\theta})$. We first consider only one vent location, V_1, and backtrack the dike trajectory, B_1, from V_1. Along such a trajectory, we identify the most likely dike nucleation point, S_1, as $p_1 = max[p(B_1)]$ and $S_1 = argmax(p(B_1))$. Consequently, p_1 gives a measure of how well the stress and dike models explain the data, that is, how consistent the stress model is with the dike nucleation zone.

Following Tarantola (2005), if we neglect model uncertainties and the data space is linear, then the likelihood function is proportional to the probability density in the data space:

$$\mathrm{P}\left(\vec{o}|\vec{\theta};\vec{\zeta}, V_1\right) \propto p\left(f_B\left(\vec{\theta};\vec{\zeta}, V_1\right)\right) = p_1 \tag{6}$$

where $\vec{\zeta}$ and V_1 are fixed. Equation 4 then becomes:

$$\mathrm{P}\left(\vec{\theta};\vec{\zeta}, V_1|\vec{o}\right) \propto p_1 \mathrm{P}\left(\vec{\theta}\right) \tag{7}$$

We now generalize the likelihood function (Equation 6) to the case of N vents:

$$\mathrm{P}\left(\vec{o}|\vec{\theta};\vec{\zeta}, V_1, \ldots, V_N\right) \propto \prod_{k=1}^{N} p_k \tag{8}$$

Table 1
Continued

Description	Symbol	Units
p shape vector	$\vec{\lambda}$	
Standard deviation	δ	
Number of forecast simulations	M^F	
Vent density	V_D	

Before further detailing the stress inversion procedure, we describe the stress and dike models used here.

2.2. Dike Propagation Model

We compute dike trajectories, both in forward and backtrack mode, with the "Simplified Analytical Model" (SAM) by Mantiloni et al. (2023a). In SAM, the dike is modeled as a penny-shaped crack with fixed radius c (or "backtrack radius," c_B, when backtracking trajectories). The crack is at all times perpendicular to the local $\vec{v}_3$ and advances in the direction of the maximum mode-I stress intensity factor, K, computed at n points along its tip-line (here $n = 12$). SAM requires a model for the stress field within the host rock, as well as the magma density, ρ_m, in addition to rock density, as inputs. The sets c, ρ_m and c_B, ρ_m constitute the dike parameters $\vec{\zeta}$ and $\vec{\zeta}^B$, respectively.

The stress intensity factor along a dike's tip-line can be expressed as a sum of two contributions (Davis et al., 2020). The first is related to the dike's volume or internal pressure, and the other is proportional to stress/pressure gradients, due to both the external stress and the density contrast between magma and host rock. The first contribution is uniform along the dike's tip-line, and in SAM it is neglected, so that K is only determined by the stress/pressure gradients (see Mantiloni et al., 2023a, Equation 5). In other words, we calculate the direction of propagation of dikes without checking whether they can actually propagate (i.e., K overcomes the fracture toughness of the host rock, K_c, as this also depends on the dike volume).

We remark that SAM in backtrack mode does not simulate downward propagation of a dike from a vent, but rather recovers the trajectory of a dike that propagated upward and reached that vent. See Mantiloni et al. (2023a) for more details and tests regarding SAM.

2.3. Stress Model

The stress field in volcanic areas is influenced by many processes. Here, we consider the often dominant contribution of gravitational loading/unloading (e.g., Heimisson et al., 2015; Mantiloni et al., 2023a; Roman & Jaupart, 2014) and focus on calderas, where this contribution is better understood (Corbi et al., 2015, 2016; Rivalta et al., 2019). We also include tectonic/regional stresses, which we assume uniform throughout the crust.

Gravitational loading/unloading arises from surface loads (e.g., topography) and subsurface density heterogeneities (e.g., the infill of a caldera). Gravitational loading and unloading are generated by volcanic processes (e.g., deposition of eruptive material, caldera collapse) and non-volcanic processes (e.g., mountain building, mass wasting, erosion, sedimentation). Loading stresses may also be altered over time due to processes such as faulting, fluid intrusions and viscous relaxation (e.g., Dieterich, 1988; Savage et al., 1992). In volcanoes, a dominant role is played by repeating dike intrusions, which tend to homogenize principal stress magnitudes by locally raising σ_3 toward σ_1 (e.g., Bagnardi et al., 2013; Chadwick & Dieterich, 1995; Corbi et al., 2015), while seismicity and viscoelasticity tend to relax shear stresses. If a topographic feature has recently formed over pre-existing topography (e.g., a new caldera depression in an older volcanic system), the newly induced gravitational stresses will be superimposed on pre-existing stresses that may have been partially homogenized, depending on the relevant time scales. Thus, the stress contribution of each topographic feature should be evaluated according to its age (Corbi et al., 2015; Maccaferri et al., 2017; Rivalta et al., 2019; Xu et al., 2017). Here we neglect these complexities, and focus on recent topographic features, assuming negligible stress change since their formation.

2.3.1. A Modular Description of Gravitational Loading

Gravitational loading/unloading is often modeled through application of positive or negative forces on a flat free surface (e.g., Dahm, 2000; J. R. Muller et al., 2001; Pinel & Jaupart, 2004) or considering the real topography (e.g., Chadwick & Dieterich, 1995; Corbi et al., 2016; McGuire & Pullen, 1989). The two approaches give similar results if the stress is evaluated deep enough below the load (e.g., Ferrante et al., 2024). Stress homogenization can also be applied in both approaches (Corbi et al., 2015; Davis et al., 2021; Heimisson et al., 2015).

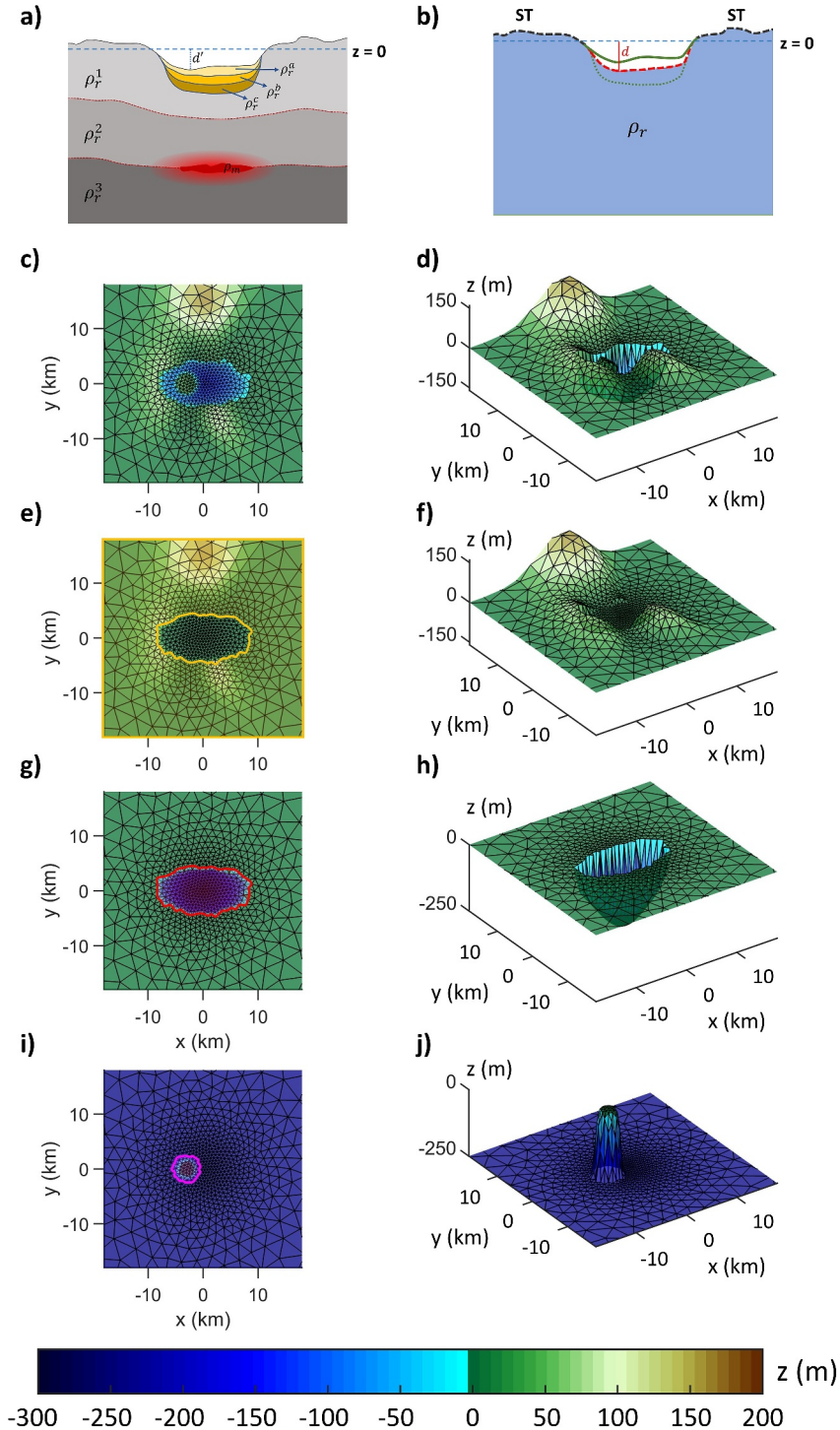

Figure 2. Single-mesh and compound-stress methods. (a) Cross section of a realistic caldera of depth d'. The melt accumulation volume and the rock layers are represented with different colors. ρ_r^i: density of different rock layers; ρ_m: magma density. (b) Compound-stress method. The topography outside the caldera is taken as Set Topography (ST). We account for the density layering by adjusting the depth d of the mesh representing the caldera. (c) Map view and (d) dimetric view of the topographic mesh employed in the "Elliptic-Caldera" scenario by Mantiloni et al. (2023a). The depth and height of the caldera and the resurgent dome are, respectively, d and h. (e) and (f) Mesh representing the Set Topography (ST, yellow). (g) and (h) "Reference caldera" (red) with depth d^{ref}. (i) and (j) "Reference dome" (purple) with height h^{ref}. Topography in dimetric views is vertically exaggerated.

Here we consider the real topography of the area and introduce the concept of "effective topography" to include the effect of local crustal density layering. Consider the example in Figure 2a, with a caldera of depth d' and a layered infill. We simulate the combined gravitational unloading of the depression and loading of the infill by adjusting the caldera floor depth into an "effective depth" d, while assuming a uniform ρ_r for the whole crust (Figure 2b). The shape of the "effective topography" may be similar enough to the current topography to be simply scaled. The "effective unloading pressure" of the caldera is then $P^U = \rho_r g d$, where g is the acceleration due to gravity. The optimal d is unknown and we aim at recovering it from the stress inversion.

Following Rivalta et al. (2019) and Mantiloni et al. (2023a), we express the stress state of a caldera as a superposition of the stresses due to recently formed topographic features ("L" for loading, "U" for unloading) and those induced by the pre-existing topography, which we refer to as "set topography" (ST), and treat as a known stress contribution:

$$\sigma_{ij}(x, y, z) = \sigma^0_{ij}(z) + \sigma^T_{ij} + \sigma^{ST}_{ij}(x, y, z) + P^U U_{ij}(x, y, z) + P^L L_{ij}(x, y, z) \quad (9)$$

where σ^0_{ij} is the unperturbed stress state before loading/unloading, here assumed as that of an unconfined half-space under the action of gravity (i.e., lithostatic: $\sigma^0_{ij}(z) = \rho_r g z \delta_{ij}$), and σ^T_{ij} represents the tectonic stresses. The gravitational loading/unloading contribution is separated into three parts as follows: $\sigma^{ST}_{ij}(x, y, z)$ is the stress associated to the ST, $P^U U_{ij}(x, y, z)$ is the unloading stress due to the formation of topographic depressions, while $P^L L_{ij}(x, y, z)$ is the loading stress due to topographic highs. $U_{ij}(x, y, z)$ and $L_{ij}(x, y, z)$ are non-dimensional functions which we assume known from the shape of the relevant topographic features, while $P^{U,L}$ are the respective unknown unloading/loading pressures, $P^U = \rho_r g d$ and $P^L = \rho_r g h$, where h is the "effective height." If multiple topographic features are present, $P^U U_{ij}$ and $P^L L_{ij}$ in Equation 9 may be repeated accordingly. We aim at retrieving d, h and σ^T_{ij}.

We compute gravitational loading/unloading stresses with two methods, which we call "single-mesh" and "compound-stress," tailored for single-purpose stress calculations and for stress parameter sampling, respectively. In both methods, we use the Boundary-Element (BE) tool *Cut and Displace* (Davis et al., 2017, 2019).

The single-mesh method is a standard approach for calculating stresses due to topographic loads. It works by representing the entire topography with a mesh of dislocations (Nikkhoo & Walter, 2015), acting as BEs, fixing a datum level (here $z = 0$, see Mantiloni et al., 2023a) and assigning to each BE stress boundary conditions so as to achieve a free surface condition (Martel & Muller, 2000; Slim et al., 2015). We create meshes using the open-source tool *DistMesh* by Persson and Strang (2004). Following Mantiloni et al. (2023a), our meshes have a diameter of 90 km, three times larger than the lateral extent of the studied region, so that their edges are distant enough from the volume where stresses are calculated. The meshes are more refined toward the center, the sides of the smallest triangular dislocations being ~800 m.

In order to avoid solving the BE problem for all combinations of the stress parameters, as required by the sampling procedure, we introduce the compound-stress method. This involves, first, calculating separate stress contributions for the different topographic features, and, second, scaling them and superposing them to retrieve an approximate stress field for any arbitrary d and h. For example, consider the synthetic scenario "Elliptic-Caldera" from Mantiloni et al. (2023a) (Figure 2c), including a caldera with a resurgent dome surrounded by gently sloping topography. The stress calculation is broken down into three parts. The ST mesh (Figure 2d) includes the topographic features outside the caldera rim. Inside the rim, the topography is flat and set to the datum level of the topography outside. The caldera mesh (Figure 2e) includes a "reference caldera" with depth d^{ref} and a flat surface at the elevation of the ST datum level outside the caldera. The resurgent dome mesh (Figure 2f) includes a "reference resurgent dome" with height h^{ref} surrounded by a flat surface at the dome datum level (the floor of the reference caldera in Figure 2e). All the meshes stem from the same "flat" mesh, as we only adjust the height of the mesh nodes from one case to another (Figures 2c, 2d, 2e and 2f). The functions U_{ij} and L_{ij} are approximated with fixed U^{ref}_{ij} and L^{ref}_{ij} calculated for d^{ref} and h^{ref}, set to the midpoint of the sampling ranges of d and h, respectively. We calculate the stresses due to each topographic feature on a grid of observation points in the subsurface and normalize them by the respective reference effective pressures; then, we scale them by the required loading/unloading pressures. Finally, all stress contributions, including tectonic stress, are added to calculate the

compound stress field. We then interpolate stresses by a linear interpolation on a 3D Delaunay triangulation (e.g., Aurenhammer et al., 2013) of the grid. Using the compound stress method in place of single-mesh calculations cuts the running time of a stress inversion by a factor of $\sim$100.

Numerical tests show that the compound-stress results are, at least in the cases we considered, an acceptable approximation: see Figure S1 of the Supporting Information S1. Stress discrepancies may diverge close to the surface, especially if prominent topographies are considered. We also note that by the design of the compound-stress calculation, the free surface condition will not be met across the topography. These are not issues here, since artifacts in the stress field near the BEs prevent calculation of SAM trajectories beyond a Minimum Distance Threshold (MDT) below the surface, which we fix to 800 m (Mantiloni et al., 2023a). Nevertheless, we recommend testing the method against single-mesh results for the end-members of any sampling range of stress parameters.

2.4. Sampling Procedure

We now explicitly define the quantities of our Bayesian approach. From Equations 4 and 8, we write Bayes' Theorem as:

$$\mathrm{P}(\vec{\theta}|\vec{o}) \propto \prod_{k=1}^{N} p_k \mathrm{P}(\vec{\theta}) \tag{10}$$

The model vector consists of up to five stress parameters:

$$\vec{\theta} = \left[d, h, \sigma_{xx}^{T}, \sigma_{yy}^{T}, \sigma_{xy}^{T}\right] \tag{11}$$

We also retrieve through post-processing the ratios R_{ij} and R_h $(i, j = x, y)$, defined as:

$$R_{xx} = \frac{\sigma_{xx}^{T}}{P^{U}}; \quad R_{yy} = \frac{\sigma_{yy}^{T}}{P^{U}}; \quad R_{xy} = \frac{\sigma_{xy}^{T}}{P^{U}}; \quad R_h = \frac{P^{L}}{P^{U}} = \frac{h}{d} \tag{12}$$

We sample $P(\vec{\theta}|\vec{o})$ by adopting the Delayed Rejection and Adaptive Metropolis Markov Chain Monte Carlo algorithm (MCMC for brevity) by Haario et al. (2006). We employ the open-source MATLAB MCMC Toolbox by Laine (2013). We fix M as the number of iterations of the MCMC algorithm. M includes an initial burn-in time, M_{burn}, to allow the MCMC to reach a stationary regime. The MCMC chain starts with a set of stress parameters drawn randomly from their respective prior distributions. Then, for each iteration, the MCMC samples a set of stress parameters as:

$$\vec{\theta}^{m} = \vec{\theta}^{m-1} + \vec{\xi} \tag{13}$$

where m is the current iteration and $\vec{\xi}$ is drawn from the proposal distribution $Q(\vec{0}, \Sigma_Q)$, that is, a multivariate normal distribution with null mean vector and diagonal covariance matrix Σ_Q. Next, we compute the stress model associated to $\vec{\theta}^{m}$ and backtrack N dike trajectories from N vents, terminating the simulations at points B_k^{end} (Section 2.1). We then interpolate each trajectory by Piecewise Cubic Hermite Interpolation (e.g., Rabbath & Corriveau, 2019), and find the point where $p(x, y, z)$ is highest, $S(r^S, z^S, \phi^S)$. Finally, we evaluate the likelihood (Equation 8). We refer to the Supporting Information S1 for additional details.

The output of the stress inversion is a set of marginal posterior PDFs for each set of the model parameters, along with the distribution of backtracked starting points, S, later employed in the forecasts, and endpoints of the backtracked trajectories, B^{end} (see Section 2.1).

2.5. Forecast Approach

We use the stress inversion results to produce a probability map of eruptive vent opening as follows:

1. We draw M^F random sets of stress ratios and the relative d from the MCMC chain, allowing for repetition. M^F corresponds to the desired number of forward dike simulations.
2. For each M^F we calculate the stress model with the compound-stress method, using the same d^{ref} and h^{ref} employed in the sampling procedure.
3. We draw M^F random starting points for the current dike trajectories from the PDFs of S. We smooth the PDFs of ϕ^S if too peaked about specific starting angles, as explained later.
4. For each of the M^F sets of stress parameters and starting points, we simulate a forward dike trajectory with SAM. We set the forward SAM radius, c, to the c_B assumed during the sampling procedure.
5. We set aside the M^F_{stop} dike trajectories which stopped before reaching the MDT from the closest dislocation of the meshed topography.
6. We stack the arrival points of the $M^F - M^F_{stop}$ dike trajectories that reach the MDT and produce a map of vent locations and fissure strikes across the caldera.
7. We calculate the vent density, V_D, as the number of vents falling within each triangle of the meshed topography, normalized by $\left(M^F - M^F_{stop}\right) * A$, A being the area of the individual triangle.
8. We visually compare the vent distributions and V_D maps to the location of vents that were not considered in the stress inversion. Future studies may introduce statistical tests to evaluate forecasts.

As shown later, the distributions of the dike starting angles, ϕ^S, may be peaked around specific values. This is because the backtracking simulations may link the few available vents to a few points of the dike nucleation zone. Arrivals of forecast trajectories starting from those points will tightly cluster around the vents. Operating in this way is equivalent to assuming that dike nucleation is favored only at specific angles, without potential physical justifications. Thus, in such cases, we smooth the ϕ^S PDFs through kernel density estimation (see, e.g., Silverman, 1986). Results will change by how the smoothing is applied, as discussed below.

2.5.1. Stress Update Forecasts

In nature, a stress-altering event may occur after the opening of all known vents, so that the sampled stress parameters correspond to a stress state preceding the alteration. Rivalta et al. (2019) and Mantiloni et al. (2021) proposed and tested a procedure to produce a forecast with updated model parameters. We further test the procedure here.

Consider the example of a caldera that is refilled by sediments after a set of vents was created. Assuming we know the sediment thickness and density, we update the stress parameters estimated on the "old" vents by shifting the MCMC chain of the d obtained from the inversion by an amount Δd corresponding to the decreased effective depth after sediment deposition, and then removing the d values that become positive after the shift. We test the forecast by comparing its results to the locations of the vents that were produced with the refilled caldera in the original scenario.

3. Testing the Stress Inversion and Vent Forecast

3.1. Stress Inversion and Forecast Set-Up

We test our stress inversion on seven out of the nine synthetic scenarios presented by Mantiloni et al. (2023a). The scenarios consider calderas with progressively more realistic topographic settings. Each scenario includes a set of dike trajectories simulated by SAM, departing from a magma storage volume below the caldera, and producing a set of N arrival points. Starting points are either equally spaced or randomly drawn along the edge of a horizontal sill, two sills at different depths, or from a vertically elongated reservoir. The dike arrival points in some scenarios lie below the surface at the MDT. All such arrival points are referred to as "vents" in the following. In one of the synthetic scenarios considered here, the dike pathways were simulated following Davis et al. (2020, 2021). In this model, which we refer to as "Three-dimensional Intrusion Model," or TIM, the 3D shape of the dike is free to change in response to external conditions and magma pressure. The dikes have a constant volume, V, and are represented by a mesh of triangular dislocations. During propagation, they advance and retreat according to the ratio between K, computed along the dike's tip-line (Davis et al., 2019), and the fracture toughness of the host rock, K_c. TIM allows for more realistic simulations of dike pathways, but requires longer running times.

For each scenario, we sort the vents into training and validation vents. We fix the Young's modulus ($E = 15$ GPa), Poisson's ratio ($\nu = 0.25$), and density $\left(\rho_r\right)$ of the host rock, as well as the magma density ($\rho_m = 2300$ kg/m^3,

Table 2
Stress Inversions: Fixed Quantities, p Distributions, Original Parameters and Results

	Fixed SAM and p parameters								
Inversion	Short name	From FS	N	c_B(km)	ρ_r (kg/m^3)	p	$\vec{\mu}$(km)	$\sqrt{\Sigma}$ (km)	$\vec{\lambda}$
Circular-caldera-Inv	CCa-I	No	8	1.2	2,500	TSD	[2, −6]	[0.6, 0.2]	-
Simplified-coastline-1-Inv	SC-1-I	No	10	0.9	2,500	TSD	[2, −6]	[1, 0.3]	-
Simplified-coastline-2-Inv	SC-2-I	Yes	10	1.2	2,500	TND	[0, 0, −6]	[1.5, 1.5, 0.25]	-
Tectonic-shear-Inv	TS-I	No	7	1.2	2,500	TSD	[2, −6]	[1.2, 0.5]	-
Refilling-caldera-Inv	RC-I	No	9	1.2	2,800	TSD	[3, −4]	[1.5, 0.3]	-
Two-reservoirs-Inv	TR-I	Yes	18	1.2	2,800	TND	[0, 0, −4]	[1.5, 1.5, 0.2]	-
Elliptic-caldera-Inv	EC-I	Yes	10	0.9	2,500	STND	[−3, 0, −4.5]	[0.5, 0.5, 1.2]	[0, 0, −5]
Complex-coastline-Inv	CCo-I	No	5	0.8	2,800	TSD	[3, −6]	[0.6, 0.2]	-

	Original stress parameters and ratios								
Scenario	d (m)	h (m)	σ^T_{xx} (MPa)	σ^T_{yy} (MPa)	σ^T_{xy} (MPa)	R_h	$R_{xx}\cdot10^{-1}$	$R_{yy}\cdot10^{-1}$	$R_{xy}\cdot10^{-1}$
Circular-caldera	−500		1.0	0.5	0		−0.82	−0.41	
Simplified-coastline	−450		1.0	1.0	0		−0.91	−0.91	
Tectonic-shear	−450		0.8	0.8	−1.0		−0.73	−0.73	0.91
Refilling-Caldera	−424		1.0	0.4	0		−0.86	−0.34	
Two-reservoirs	−424		1.0	0.4	0		−0.86	−0.34	
Elliptic-caldera	−150	150	1.0	0.6	0	−1.0	−2.72	−1.63	
Complex-coastline	−424		1.0	0.4	0		−0.86	−0.34	
Inversion	d (m)	h (m)	σ^T_{xx} (MPa)	σ^T_{yy} (MPa)	σ^T_{xy} (MPa)	R_h	$R_{xx}\cdot10^{-1}$	$R_{yy}\cdot10^{-1}$	$R_{xy}\cdot10^{-1}$
Median values from stress inversions									
CCa-I	−780		1.6	0.8			−0.82	−0.44	
SC-1-I	−1720		2.8	3.0			−0.70	−0.71	
SC-2-I	−490		1.1	0.9			−0.99	−0.74	
TS-I	−590		0.9	0.9	−1.1		−0.57	−0.57	0.68
RC-I	−340		1.0	0.9			−1.03	−0.89	
TR-I	−940		1.0	1.0			−0.41	−0.40	
EC-I	−250	220	1.5	1.3		−0.9	−2.40	−2.06	
CCo-I	−500		1.1	1.1			−0.73	−0.72	
Standard deviation (δ)									
CCa-I	220		0.4	0.3			0.09	0.09	
SC-1-I	320		0.6	0.7			0.14	0.10	
SC-2-I	150		0.4	0.5			0.26	0.37	
TS-I	270		0.4	0.4	1.0		0.38	0.41	0.72
RC-I	110		0.4	0.4			0.42	0.47	
TR-I	360		0.6	0.6			0.50	0.46	
EC-I	70	100	0.4	0.6		0.2	0.91	1.01	
CCo-I	320		0.6	0.6			0.82	0.78	

Note. FS (Free Surface): if "Yes," dike trajectories are backtracked from vents on the free surface; otherwise, from points at or near the Minimum Distance Threshold.

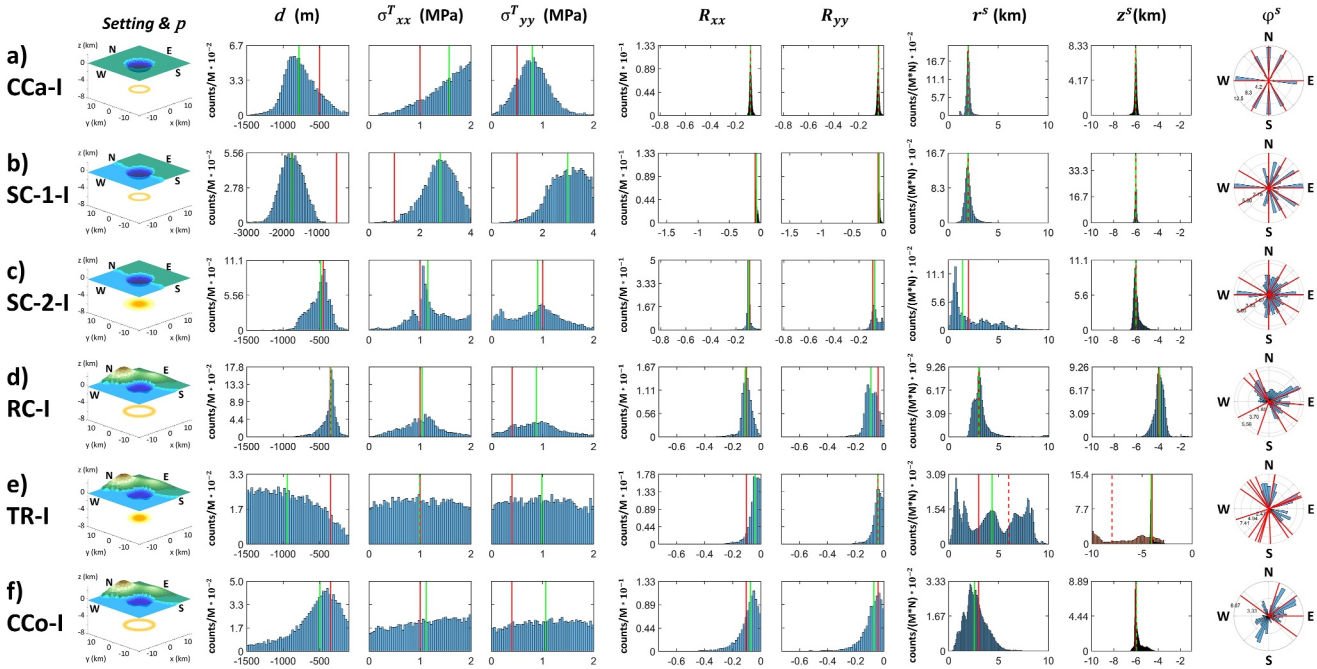

Figure 3. Stress inversion results (continues in Figure 4). Each row corresponds to one stress inversion, as indicated on the left. From left to right: view of the topographic setting together with a diagram of the type of p (Section 3.1); posterior PDFs of the stress parameters and their ratios; PDFs of the dike starting points coordinates (r^S, z^S, ϕ^S). $M' = M - M_{burn}$, as the burn-in time steps are discarded from the MCMC chain. Red lines mark the originally assigned value of the parameter or starting points coordinates (Mantiloni et al., 2023a); green lines mark the median of the PDFs. In Two-Reservoirs-Inv, dotted red lines mark the radius and depth of the deep reservoir neglected in the inversion, and the plot of the z^S PDF includes the distribution of the vertical coordinates of the points where backward SAM trajectories stop (B^{end}, orange bins), to be compared with the depth of the neglected reservoir (dotted red line).

unless specified otherwise). Here, we do not explore the effects of introducing bias in any of these parameters. Mantiloni et al. (2023a) calculated the scenario trajectories using $c = 1200$ m. In our stress inversions, we use both $c_B = c$, to verify whether, by using the same exact dike propagation model, we recover unbiased stresses, and $c_B \neq c$, to test a less favorable case (Table 2). Moreover, we fix the horizontal and vertical thresholds where backtracked dike trajectories are stopped to $r = 10$ km, $z = -10$ km.

To describe the dike nucleation zone, we assume a p that may be the same as, similar to, or different from the p used to create the scenarios. We consider different formulations for p to describe situations where the highest probability to nucleate a dike is at the center of a spherical reservoir, around the edge of a sill-shaped reservoir, or at the center of a vertically elongated reservoir. These are, respectively, a trivariate normal distribution (TND), a torus-shaped distribution (TSD) and a skewed, trivariate normal distribution (STND) (Figure 1c). They are all described by a mean $\vec{\mu}$, a covariance matrix Σ and shape parameters $\vec{\lambda}$. Their mathematical expressions are reported in the Supporting Information S1.

We fix the number of MCMC iterations as $M = 20,000$, with $M_{burn} = 2,000$. We assign uniform prior PDFs ($P(\vec{\theta})$, see Equation 10) for the stress parameters. We initially take Σ_Q of the proposal distribution (Equation 13) as an identity matrix, and let it be adapted during the MCMC (see Haario et al., 2006). More details about the choice of M can be found in the Supporting Information S1.

We report the results of our stress inversions in Table 2, Figures 3 and 4. We quantify the performance of the inversions by comparing the medians of the stress parameters' posterior PDFs to their respective original values and the spread of the PDFs, in terms of standard deviation. We remark that the tails of the actual posterior PDFs may extend beyond the sampling range when they have large spread. In such cases, the medians we discuss are only representative of the truncated distributions within our sampling ranges. Finally, we run forecasts on the four stress inversion tests that we deem most instructive, always fixing $M^F = M$ (Figure 5).

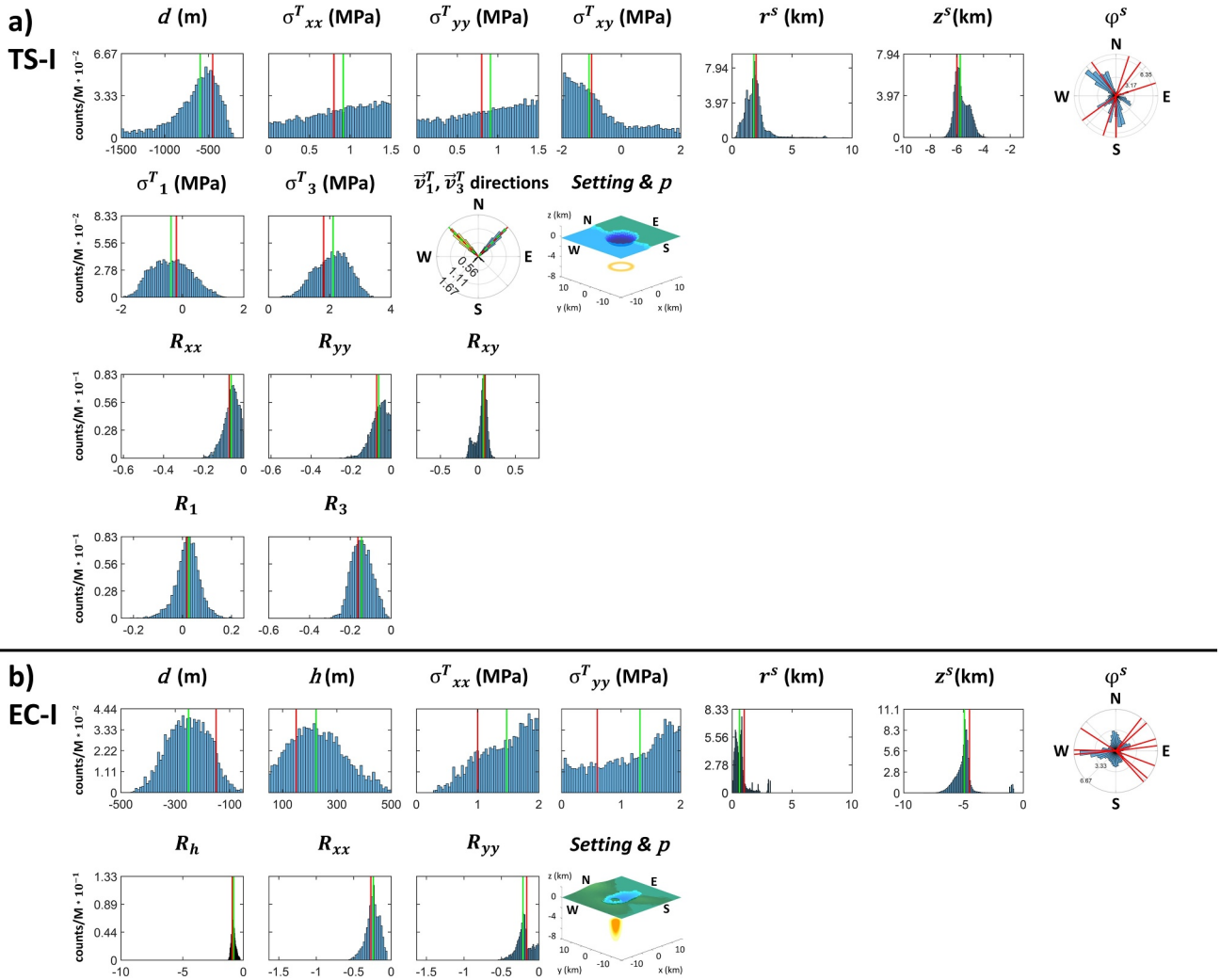

Figure 4. Stress inversion results for tests considering four stress parameters. (a) Tectonic-Shear-Inv. From top to bottom, posterior PDFs of four stress parameters and the coordinates of the dike starting points (r^S, z^S, ϕ^S), PDFs of the magnitude (σ_1^T, σ_3^T) and direction $(\vec{v}_1^T, \vec{v}_3^T)$ of tectonic principal stresses, as well as a view of the topographic setting with a diagram of the type of p, PDFs of the stress ratios, PDFs of the ratios between σ_1^T, σ_3^T and $\rho_r g d$. (b) Elliptic-Caldera-Inv. From top to bottom: PDFs of four stress parameters and the coordinates of the dike starting points (r^S, z^S, ϕ^S), PDFs of the stress ratios as well as a view of the topographic setting with a diagram of the type of p. $M' = M - M_{burn}$, as the burn-in time steps are discarded from the MCMC chain. Red lines mark the originally assigned value of the parameter or the coordinates of the dike starting points (Mantiloni et al., 2023a); green lines mark the median of the PDFs.

3.2. Stress Inversion and Forecast Results Using Synthetic Scenarios

3.2.1. Detailed Analysis of Results

The first stress inversion, "Circular-Caldera-Inv" (CCa-I, Figure 3a), which involves a circular caldera with a flat free surface, is a "dummy test" where assumptions on dike parameters and nucleation zone closely reflect the original scenario settings (Table 2). The inversion well constrains the ratios between tectonic stresses and unloading pressure (R_{xx}, R_{yy}) (PDFs are peaked around unbiased values, Table 2). In contrast, the individual stress parameters are either unconstrained (no evident peak) or peaked around biased values. The coordinates of the dike starting points (r^S, z^S, ϕ^S) are remarkably well retrieved (Figure 3a). This test suggests that, if uncertainty in dike parameters and dike nucleation zone is small, then the ratios of stress parameters are constrained accurately. This replicates a result obtained by Rivalta et al. (2019) and Mantiloni et al. (2021) in 2D settings.

In the "Simplified-Coastline" scenario, a step-like coastline divides the topography into two flat regions of different elevation. We use this scenario to test two biased assumptions. First, we take $c_B \neq c$ ("Simplified-

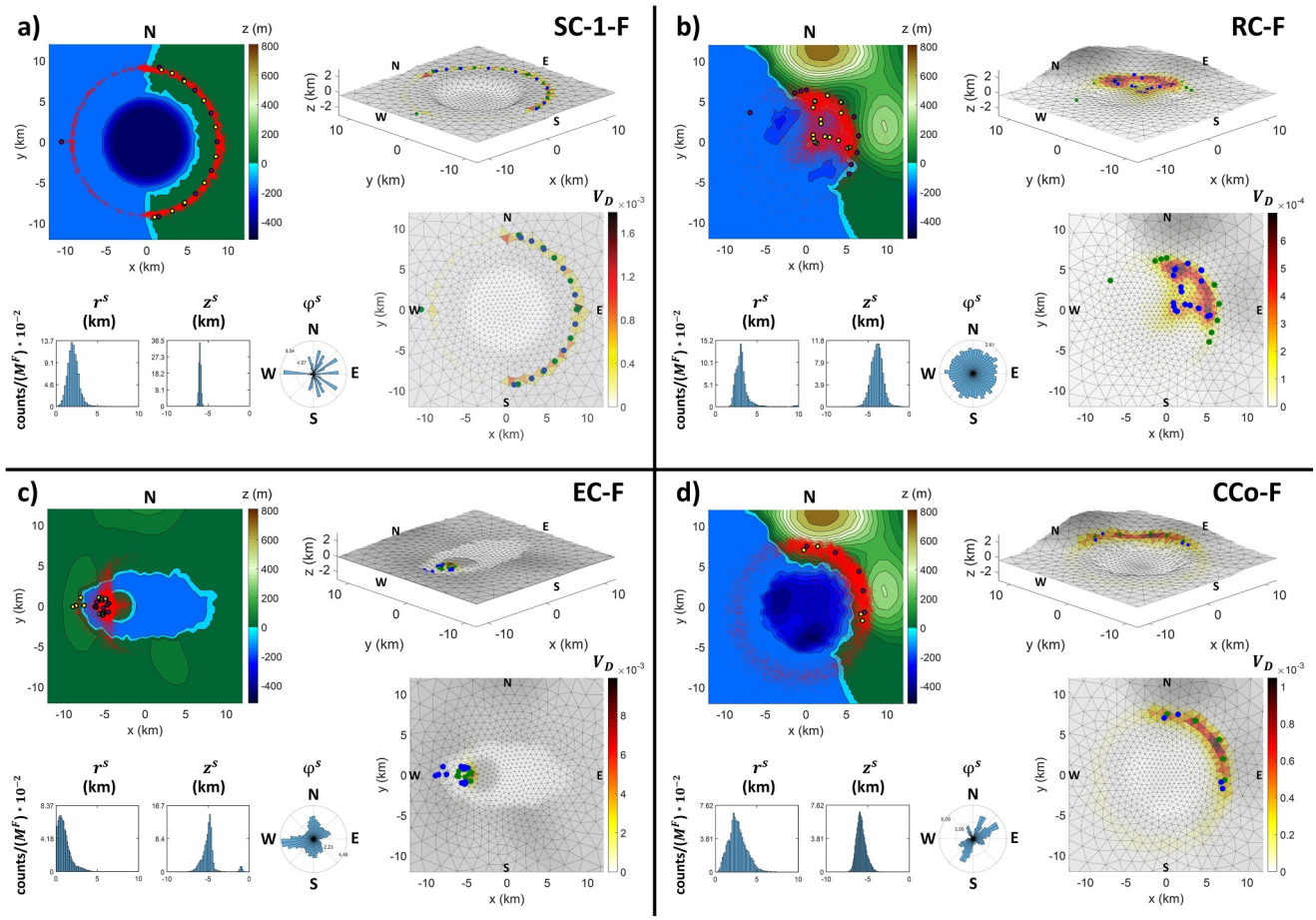

Figure 5. Vent forecast results. Each panel includes, from the top-left corner clockwise: map view of the vents simulated during the forecast and their strikes (red segments), superimposed on an elevation map of the synthetic caldera; dimetric view of the vent density (V_D) map and topography mesh; map view of V_D with color scale; distributions of the cylindrical coordinates of the dike starting points employed in the SAM simulations, to be compared to the starting points retrieved from the stress inversions (Figures 3 and 4). Training vents are in green/purple, validation vents in blue/yellow.

Coastline-1-Inv" or SC-1-I, Figure 3b). Then, we backtrack dikes from the free surface and assume a p that does not match well the original dike starting points ("Simplified-Coastline-2-Inv" or SC-2-I, Figure 3c). In spite of these more unfavorable assumptions, the stress parameter ratios are all well constrained. The individual stress parameters are well constrained in SC-2-I, although the PDF of σ_{yy} and R_{yy} are comparatively more spread-out (Table 2). In contrast, using $c_B \neq c$ in SC-1-I biases the stresses (Figure 3b, Table 2). The PDFs of dike starting coordinates are well constrained, especially their z^S (Figures 3b and 3c). These tests show that adding uncertainties or bias to our assumptions leads to more unconstrained or biased posterior PDFs. They also show that with more realistic, non-axisymmetric topographies, and accurate assumptions on fixed parameters, the individual stress parameters, besides the ratios, may also be well constrained.

We use the results of SC-1-I to run a forecast ("Simplified-Coastline-1-For" or SC-1-F, Figure 5a). High values of vent density (V_D) cluster around the training vents, but not as much around the validation vents. This strong dependence on the starting locations of past dikes may be undesirable; thus, in later forecasts we test the procedure of smoothing the PDF of ϕ^S. A side-effect of the biased recovered stresses is that most dikes (roughly three out of four rather than a few as in the original model, or one out of 10, as in the forecasts discussed later) stop in the subsurface if the original $\rho_m = 2300$ kg/m^3 is employed. If we lower ρ_m, the fraction of stopped dikes decreases, but the vent distribution shifts a little. This may be the reason why in Figure 5a, where we used $\rho_m = 2100$ kg/m^3, the highest expected vent density on the sea side is close to, but does not include, the only offshore vent. This discrepancy may also be due to uncertainties linked to the compound-stress method, or a trade-off between stress parameters and magma density that needs to be better investigated.

The "Tectonic-Shear" scenario maintains the topography of Simplified-Coastline, but considers a rotated tectonic stress tensor $\left(\sigma_{xy}^{T} \neq 0\right)$. Thus, in "Tectonic-Shear-Inv" (TS-I, Figure 4a), we consider four stress parameters. Assumptions on p and c_B coincide with the original scenario, so that we expect all parameters to be retrieved without bias. The depth d and the ratios R_{xx}, R_{yy}, R_{xy} are well constrained (Figure 4a, Table 2). While the retrieved tectonic stress components have rather flat distributions, the tectonic principal stress magnitudes (σ_1^T and σ_3^T), and, especially, their directions are accurately constrained. The ratios R_1^T, R_3^T between σ_1^T, σ_3^T and the caldera unloading pressure $\left(\rho_r g d\right)$, respectively, are also well constrained. r^S and z^S are rather well constrained, while ϕ^S are poorly constrained.

The "Refilling-Caldera" scenario considers a caldera lying on a coastline with a complex caldera floor and a hill range on the mainland. The validation vents were produced with a modified setting, where the caldera is partially refilled. We use the vents produced before the caldera refilling to run the stress inversion ("Refilling-Caldera-Inv" or RC-I), while in the forecast ("Refilling-Caldera-For" or RC-F) we update the stress by shifting the chain of d by an appropriate amount (Section 2.5.1). The p assumed for the dike nucleation zone matches the original model, but has a larger spread than the ones considered in the previous inversions (Table 2). As shown in Figure 3d and Table 2, d is well-constrained, while the PDFs of σ_{xx} and σ_{yy} are spread-out; σ_{yy} and R_{yy} are particularly poorly constrained. The PDFs of r^S and z^S are more spread-out than in CCa-I and SC-1-I, but peaked around the original values (Figure 3d). The PDF of ϕ^S are not as peaked around the starting angles as they are in previous cases. In the forecast (RC-F, Figure 5b), vents simulated with the updated stresses (red segments) cluster along the north-eastern rim of the caldera and around the caldera center, where a mild topographic relief is present, matching the locations of validation vents (yellow/blue dots in Figure 5b). These results are obtained by smoothing the ϕ^S PDF from RC-I to a roughly uniform distribution. If the ϕ^S PDF is not smoothed, the V_D map fails to reproduce the distribution of validation vents (not shown in Figure 5b); this is expected, because validation vents had different starting angles than training vents.

In "Two-Reservoirs," the topography is the same as in "Refilled-Caldera," but the original dikes started from two sill-like reservoirs with different radii located at different depths. In "Two-Reservoirs-Inv" (TR-I, Figure 3e), the assumed p only includes, and matches, the shallow reservoir. Consequently, the inversion fails to constrain any stress parameter, whereas the z^S of the shallow reservoir is constrained very well. By looking at the distribution of depths where SAM trajectories stop $\left(B^{end}\right)$ in the MCMC (see the z^S PDF panel for TR-I, Figure 3e), we notice that it has a peak about the 10-km depth threshold, not far from the depth of the neglected reservoir. The starting radius, r^S, is ill-constrained, as its PDF displays secondary peaks, one of which is close to the radius of the ignored reservoir (Figure 3e). This highlights how the distributions of S and B^{end} provide posterior information that could be used to improve our assumption about p in a successive inversion. Future work may test if subsequent MCMC chains, where p is updated progressively, lead to the algorithm converging to stable distributions. Moreover, in a general case, if the distribution of B^{end} and the PDF of z^S resemble each other, the assumption on p is more likely to be accurate, since SAM trajectories stop in the dike nucleation zone rather than only cutting through it. This is verified in Figure S5 of the Supporting Information S1, which includes all distributions of S and B^{end}.

Considering an additional topographic feature adds a further source of uncertainty to our tests. The "Elliptic-Caldera" scenario (Section 2.3 and Figure 2c) includes a resurgent dome within an elliptic caldera surrounded by mild topographic highs. Dike starting points are drawn from a vertically elongated reservoir, with higher nucleation chances at shallower depths (Mantiloni et al., 2023a). In "Elliptic-Caldera-Inv" (EC-I, Figure 4b), we consider the height h of the resurgent dome as an additional stress parameter, and assume a p that is skewed toward the surface (STND, see Figure 1c). The assumptions in the stress inversion are all unfavorable, as we backtrack dikes from the free surface and take $c_B \neq c$ (Table 2). Nonetheless, the ratios are well constrained, R_h being recovered remarkably well (Figure 4b and Table 2). The inversion performs much worse on the individual parameters. In particular, d and h are biased in a similar way to SC-1-I, as they are peaked far from the original values, while the tectonic stress components are unconstrained. In this case, contrary to SC-1-I, we deem that the bias in d and h is mostly due to the choice of p and the application of the compound-stress method to a more complex topography (see the Supporting Information S1). Indeed, the vertically elongated p may be equally well-intercepted by dike trajectories calculated with different stress parameters, which adds uncertainty to the parameters. Both r^S and z^S are well constrained, even though the PDF of r^S shows multiple closely spaced peaks. On the other hand, the inversion generally fails to constrain ϕ^S, as shown in Figure 4b. We run the third forecast,

"Elliptic-Caldera-For" (EC-F), on the results of this inversion. We maintain the PDF of ϕ^S from the inversion, but we smooth the PDF of r^S to cut out the thin peaks (Figure 4b). As illustrated in Figure 5c, simulated vents cluster in the western side of the resurgent dome and, to a much lesser extent, along the western rim of the elliptic caldera, but most of the training and validation vents fall short of the highest V_D area. The main reason for such a discrepancy, besides the compound-stress approximation, is that, in the original scenario by Mantiloni et al. (2023a), all dikes started at a fixed radial distance from the axis of the reservoir, contrarily to what assumed in the forecast.

We run the last stress inversion on the "Complex-Coastline" scenario, where the dike trajectories and vents are produced by TIM and start from equally spaced points at the edge of a sill (Mantiloni et al., 2023a; Figure 4a). In "Complex-Coastline-Inv" (CCo-I), we assume a p that well matches the reservoir in the original model. Mantiloni et al. (2023a) discussed how the accuracy of SAM in backtracking TIM pathways improves if c_B is calibrated according to the volumes of TIM dikes ($2 \cdot 10^6 - 10^7$ m^3 in the original model). Here we assume $c_B = 800$ m, close to the optimal $c_B = 880$ m estimated by Mantiloni et al. (2023a). As seen from Figure 3f and Table 2, the PDFs for R_{xx}, R_{yy} are peaked not far from the original values. Moreover, the inversion is successful in constraining d, but fails to constrain the tectonic stress components. Both r^S and z^S are well constrained, but the PDF of r^S is very spread-out. Only two of the original dike starting angles are well constrained in the PDF of ϕ^S (Figure 3f). We use the results of this inversion to run the last forecast, "Complex-Coastline-For" (Cco-F), displayed in Figure 5d. The distribution of simulated vents is scattered, with many vents falling within the caldera. The high V_D areas, nonetheless, match the locations of the original vents.

3.2.2. Main Results

A common result in the inversions is that, with the exception of TR-I, whose p was very different from what used to generate the data, the amount of unloading, represented by the effective depth of the caldera, d, is usually well constrained (Table 2). Secondly, the ratios between stress parameters are always well constrained and usually unbiased, except again for TR-I. This is the main factor behind the accuracy of the forecasts, as the dike trajectories' curvature is determined by the stress ratios and d. The magnitudes and orientations of tectonic stresses are generally well constrained, unless the topography is axisymmetric (CCa-I); this is the case even when the Cartesian components of the tectonic stress tensor are not (TS-I). Results deteriorate when the vents of the training set are all clustered on one side of the caldera (e.g., CCo-I, where all vents lie on the mainland, see Figure 5d). In tests not included here, SC-2-I and RC-I performed much worse when the offshore vents were not included in the training sets.

Fixing $c_B \neq c$ biases the results of very simple scenarios (e.g., SC-1-I, with a simplistic topography and a p reflecting the original dike nucleation zone, Figure 3b). However, this issue is not as significant in more complex scenarios, such as EC-I, where other sources of uncertainty (multiple topographic elements, backtracking dikes from the free surface) play a larger role.

The choice of p has generally the largest control on the inversion results. In general, more vertically spread p lead to more uncertainty in the stress parameters and dike starting points, so that it is important to not overstate uncertainties when defining p. Underestimating uncertainties is equally undesirable: for instance, choosing a p with minimal vertical spread means that dike pathways will cross volumes of high probability only for very specific stress parameters, and the estimated parameter uncertainties may be too small. Thus, assigning p requires careful thought.

In the forecasts, assuming a broader distribution of starting depths, z^S, translates into a broader distribution of simulated vents. To quantify such sensitivity, we simulated forward dike pathways with SAM in the "Circular-Caldera" scenario varying the starting depth of dikes for a fixed stress model, and found that a difference of 1 km in starting depth leads to a $\sim$600 m horizontal distance between the resulting vents. This distance, however, depends on the caldera geometry, which determines the intensity of the unloading effect, and the starting depth itself.

4. Discussion

In this work, we outline a new framework to determine the stress state of volcanoes, constrained by the locations of past eruptive vents and information on the magma reservoir. The framework can then be used to estimate the

spatial probability of future vent opening. Tests on synthetic data produced by Mantiloni et al. (2023a) reveal a number of features and identify pathways for further testing and development.

4.1. Trade-Offs and Uncertainties

Several uncertainties and parameter trade-offs affect the results of our synthetic tests. Assumptions about the dike nucleation zone (D) have a large influence. Choosing a probability density function for D requires estimates of the depth and geometry of the magma storage, which may be provided by inversion of ground deformation data, seismic tomography, and petrological studies. A deeper understanding of the conditions that promote or hinder dike nucleation is also necessary. Previous studies in this direction, such as McLeod and Tait (1999); Gudmundsson (2006); Grosfils (2007); Chestler and Grosfils (2013), can help inform the choice of p. We assumed that the dike nucleation zone had not changed significantly over time, which is a condition that may often apply for calderas but not for all volcanic systems.

Our results show how stress inversions may fail if the assumption on the dike nucleation zone does not match the actual magma plumbing system. However, the stress inversion might still help better constrain the location and geometry of the magma reservoir, by exploiting the "posterior" distribution of the stopping points of backtracked dike trajectories resulting from the inversion. The presence of multiple reservoirs can also be considered, provided separate sets of eruptive vents can be associated with their parent reservoir (e.g., by studying magma composition). In this respect, our approach could help constrain cases where the existence of multiple reservoirs is debated (e.g., Baker & Amelung, 2012).

A source of uncertainty in the forecast arises from fixing the magma density (ρ_m), as it controls, together with stress gradients in the rock, the crack driving pressure in SAM. Different assumptions about ρ_m lead to different probability maps. One solution in future applications may be to treat ρ_m probabilistically; for instance, assigning it a PDF according to some prior knowledge, or as an additional free parameter.

Minor effects are given by the size of SAM dikes, which trades off with the stress parameters and ratios. This is more evident in simplified settings and when the uncertainty on the vertical size of the dike nucleation zone is small. Thus, the effect this would have in nature is not clear and, again, further testing is needed.

4.2. Applications to Nature

The synthetic scenarios considered here span a range of caldera settings: Refilling-Caldera resembles the topography of Campi Flegrei (e.g., Di Vito et al., 2016; Orsi et al., 1996), while the morphology of Elliptic-Caldera is similar to that of Long Valley Caldera (e.g., Hildreth, 2004). However, they cannot represent the wide variability of real calderas. Applications to specific calderas may benefit from dedicated synthetic and sensitivity tests before running any stress inversion.

Well-established approaches to probability maps of future vent opening (Bevilacqua et al., 2015; Connor & Hill, 1995; Selva et al., 2012) rely on the assumption that future vents are more likely to open where more past vents are found. Thus, if some past vents are missing from the record, the corresponding areas will be assigned a lower probability. Our tests show that, if vents from large caldera sectors are entirely excluded from the training set, stress inversion and forecast results may worsen considerably. Conversely, if at least a few vents are available for all caldera sectors, results are still reliable even with smaller training sets. Thus, we deem our method to be less sensitive to eruptive vents missing from the record than purely statistical methods.

Applying our strategy to real scenarios will entail many further challenges. First, the dike propagation and stress models we adopt require extensive testing with real data. We remark, however, that stress models relying on the same principles and assumptions have been successfully applied to explain vent patterns in many volcanic settings, including calderas (Chadwick & Dieterich, 1995; Corbi et al., 2015), shifting volcanism (Neri et al., 2018), and complex dike pathways (Davis et al., 2021).

Some of the neglected factors (e.g., rock heterogeneities) may be inherently accounted for in the retrieved PDFs of our stress inversions, which are expected to map many different effects onto "effective" stress parameters. This may result in biased PDFs (e.g., underestimated caldera unloading), without hindering the quality of the forecasts. An application of the "effective stress model" principle was shown in 2D by Mantiloni et al. (2021) by running stress inversions on layered gelatin blocks while assuming a homogeneous medium.

The effect of pre-existing structures on the crustal stress field is neglected in our models. Dikes and faults can interact with each other through the stresses they induce (e.g., Maccaferri et al., 2017; Maccaferri et al., 2014, Supporting Information). In principle, such effects could be included in our models, but the geometry of pre-existing faults at depth is usually poorly constrained. Consequently, assuming the presence of such faults in a stress inversion may further bias the results. Similarly, dikes modify the stress field while they advance (Kühn & Dahm, 2008); hence, a dike can influence other dikes' pathways, whether it was emplaced before them, or they propagate simultaneously. Dike-to-dike interaction, as well as interaction with rock volumes where previous intrusions have accumulated, will be explored in a future study.

Our approach may capture the cumulative stress modifications from past eruptions, such as caldera refilling, by constraining the "average" stress states associated to distinct epochs of volcanic activity. This can be done by running distinct stress inversions with vents from specific epochs. Nonetheless, our stress model does not take into account stress modifications over time due to processes such as viscoelasticity and repeated dike intrusions. Such processes may have a large influence around reservoirs or in large, heavily intruded volcanic edifices. Thus, further developments are needed before our stress model can be applied to such settings.

We do not include uncertainty on the vent locations. In future applications, we may model it by assigning a PDF to each vent. Orientations of past eruptive fissures and earthquake focal mechanisms may also help better constrain stress. Dikes that stopped before producing a vent, but are exposed or geophysically constrained, may also be included in our approach. Accounting for the influence of factors such as surface faulting and complex rheology in the shallow crust, as well as the process of vent opening and construction, are all points for future developments to clarify the interplay between dike propagation and the Earth's surface.

The stress inversion framework we have outlined here has potential applications beyond volcanology. Accurate models of the stress field are critical to anticipate the characteristics of hydraulic fracturing (e.g., Busetti & Reches, 2014), wellbore failure (Wiprut & Zoback, 2000), and reservoir stability under fluid injection or extraction (Martínez-Garzón et al., 2013). Geothermal exploration and production are also dependent on accurate assessment of subsurface stresses (Cloetingh et al., 2010), and many geothermal fields lie in active volcanic systems (Bertani, 2016; Nielsen et al., 2000). Finally, the design and construction of underground storage facilities for the disposal of hazardous waste (e.g., Jo et al., 2019) also rely on assessing the stress state of the host rock. Thus, the development of stress inversion methods such as the present one may lead to a more efficient and safer exploitation of natural resources.

5. Conclusions

In this work, we introduce a framework to constrain the tectonic and topographic contributions to the three-dimensional stress state of calderas on the basis of the locations of past eruptive vents and independent information on the zones of dike nucleation at depth. We then illustrate how to use the recovered stress state to produce probability maps of future vent opening locations, testing the framework on synthetic scenarios. The stress inversions are mainly influenced by uncertainty in the location and size of the magma reservoir, and assumptions on the dike size, magma and rock density. Nonetheless, the ratios between the tectonic and gravitational stresses are generally well constrained by the stress inversions, and vent forecasts successfully identify areas of high probability of vent opening. With further testing and developments, our approach could be extended to other volcanic settings, and help constrain crustal stresses in other geophysical problems.

Data Availability Statement

The open-source software *DistMesh* is found from Persson and Strang (2004). The open-source Boundary-Element tool *Cut and Displace* is found from Davis (2020). The code for SAM and the data of the synthetic scenarios are available from Mantiloni et al. (2023b). The codes for running the stress inversion and the eruptive vent forecast, as well as the results of the synthetic tests presented here, are available from Mantiloni et al. (2024).

Acknowledgments
We are grateful to Virginie Pinel, Mehdi Nikkhoo, Francesco Maccaferri, and Torsten Dahm for constructive discussion and support. We also thank Marco Bagnardi and two anonymous reviewers, whose feedback has significantly improved the clarity of the work. L. M. is funded by the DFG Grant N. RI 2782/6-1-ZO 277/3-1 within the MagmaPropagator project. T. D. received funding from the European Research Council under Horizon 2020 research and innovation program Grant agreement 772255. Any use of trade, firm, or product names is for descriptive purposes only and does not imply endorsement by the U.S. Government. Open Access funding enabled and organized by Projekt DEAL.

References

Anderson, E. M. (1937). Ix.—The dynamics of the formation of cone-sheets, ring-dykes, and caldron-subsidences. *Proceedings of the Royal Society of Edinburgh*, *56*, 128–157. https://doi.org/10.1017/s0370164600014954

Aurenhammer, F., Klein, R., & Lee, D.-T. (2013). *Voronoi diagrams and Delaunay triangulations*. World Scientific Publishing Company.

Bagnardi, M., Amelung, F., & Poland, M. P. (2013). A new model for the growth of basaltic shields based on deformation of Fernandina volcano, Galápagos Islands. *Earth and Planetary Science Letters*, *377*, 358–366. https://doi.org/10.1016/j.epsl.2013.07.016

Baker, S., & Amelung, F. (2012). Top-down inflation and deflation at the summit of Kīlauea volcano, Hawaii observed with InSAR. *Journal of Geophysical Research*, *117*(B12). https://doi.org/10.1029/2011jb009123

Bertani, R. (2016). Geothermal power generation in the world 2010–2014 update report. *Geothermics*, *60*, 31–43. https://doi.org/10.1016/j.geothermics.2015.11.003

Bevilacqua, A., Isaia, R., Neri, A., Vitale, S., Aspinall, W. P., Bisson, M., et al. (2015). Quantifying volcanic hazard at Campi Flegrei Caldera (Italy) with uncertainty assessment: 1. Vent opening maps. *Journal of Geophysical Research: Solid Earth*, *120*(4), 2309–2329. https://doi.org/10.1002/2014JB011775

Busetti, S., & Reches, Z. (2014). Geomechanics of hydraulic fracturing microseismicity: Part 2. Stress state determination. *AAPG Bulletin*, *98*(11), 2459–2476.

Chadwick, W. W., & Dieterich, J. H. (1995). Mechanical modeling of circumferential and radial dike intrusion on Galápagos volcanoes. *Journal of Volcanology and Geothermal Research*, *66*(1–4), 37–52. https://doi.org/10.1016/0377-0273(94)00060-t

Chestler, S. R., & Grosfils, E. B. (2013). Using numerical modeling to explore the origin of intrusion patterns on Fernandina volcano, Galápagos Islands, Ecuador. *Geophysical Research Letters*, *40*(17), 4565–4569. https://doi.org/10.1002/grl.50833

Cloetingh, S., van Wees, J. D., Ziegler, P., Lenkey, L., Beekman, F., Tesauro, M., et al. (2010). Lithosphere tectonics and thermo-mechanical properties: An integrated modelling approach for enhanced geothermal systems exploration in Europe. *Earth-Science Reviews*, *102*(3–4), 159–206. https://doi.org/10.1016/j.earscirev.2010.05.003

Connor, C. B., & Hill, B. E. (1995). Three nonhomogeneous Poisson models for the probability of basaltic volcanism: Application to the Yucca mountain region, Nevada. *Journal of Geophysical Research*, *100*(B6), 10107–10125. https://doi.org/10.1029/95JB01055

Corbi, F., Rivalta, E., Pinel, V., Maccaferri, F., & Acocella, V. (2016). Understanding the link between circumferential dikes and eruptive fissures around calderas based on numerical and analog models. *Geophysical Research Letters*, *43*(12), 6212–6219. https://doi.org/10.1002/2016gl068721

Corbi, F., Rivalta, E., Pinel, V., Maccaferri, F., Bagnardi, M., & Acocella, V. (2015). How caldera collapse shapes the shallow emplacement and transfer of magma in active volcanoes. *Earth and Planetary Science Letters*, *431*, 287–293. https://doi.org/10.1016/j.epsl.2015.09.028

Currenti, G., Napoli, R., Coco, A., & Privitera, E. (2017). Effects of hydrothermal unrest on stress and deformation: Insights from numerical modeling and application to Vulcano Island (Italy). *Bulletin of Volcanology*, *79*(4), 28. https://doi.org/10.1007/s00445-017-1110-3

Dahm, T. (2000). Numerical simulations of the propagation path and the arrest of fluid-filled fractures in the Earth. *Geophysical Journal International*, *141*(3), 623–638. https://doi.org/10.1046/j.1365-246x.2000.00102.x

Davis, T. (2020). Timmmdavis/CutAndDisplace: Getting a DOI (1.1) [Software]. *Zenodo*. https://zenodo.org/records/3694164

Davis, T., Bagnardi, M., Lundgren, P., & Rivalta, E. (2021). Extreme curvature of shallow magma pathways controlled by competing stresses: Insights from the 2018 Sierra Negra eruption. *Geophysical Research Letters*, *48*(13), e2021GL093038. https://doi.org/10.1029/2021gl093038

Davis, T., Healy, D., Bubeck, A., & Walker, R. (2017). Stress concentrations around voids in three dimensions: The roots of failure. *Journal of Structural Geology*, *102*, 193–207. https://doi.org/10.1016/j.jsg.2017.07.013

Davis, T., Healy, D., & Rivalta, E. (2019). Slip on wavy frictional faults: Is the 3rd dimension a sticking point? *Journal of Structural Geology*, *119*, 33–49. https://doi.org/10.1016/j.jsg.2018.11.009

Davis, T., Rivalta, E., & Dahm, T. (2020). Critical fluid injection volumes for uncontrolled fracture ascent. *Geophysical Research Letters*, *47*(14), e2020GL087774. https://doi.org/10.1029/2020GL087774

Del Negro, C., Currenti, G., & Scandura, D. (2009). Temperature-dependent viscoelastic modeling of ground deformation: Application to Etna volcano during the 1993–1997 inflation period. *Physics of the Earth and Planetary Interiors*, *172*(3–4), 299–309. https://doi.org/10.1016/j.pepi.2008.10.019

Dieterich, J. H. (1988). Growth and persistence of Hawaiian volcanic rift zones. *Journal of Geophysical Research*, *93*(B5), 4258–4270. https://doi.org/10.1002/9781118782064.ch13

Di Vito, M. A., Acocella, V., Aiello, G., Barra, D., Battaglia, M., Carandente, A., et al. (2016). Magma transfer at Campi Flegrei caldera (Italy) before the 1538 AD eruption. *Scientific Reports*, *6*(1), 32245. https://doi.org/10.1038/srep32245

Ferrante, G., Rivalta, E., & Maccaferri, F. (2024). Spatio-temporal evolution of rift volcanism controlled top-down by a deepening Graben. *Earth and Planetary Science Letters*, *629*, 118593. https://doi.org/10.1016/j.epsl.2024.118593

Fournier, N., & Chardot, L. (2012). Understanding volcano hydrothermal unrest from geodetic observations: Insights from numerical modeling and application to White Island volcano, New Zealand. *Journal of Geophysical Research*, *117*(B11). https://doi.org/10.1029/2012jb009469

Gelman, A., Carlin, J. B., Stern, H. S., Dunson, D. B., Vehtari, A., & Rubin, D. B. (2013). *Bayesian data analysis*. CRC Press.

Grosfils, E. B. (2007). Magma reservoir failure on the terrestrial planets: Assessing the importance of gravitational loading in simple elastic models. *Journal of Volcanology and Geothermal Research*, *166*(2), 47–75. https://doi.org/10.1016/j.jvolgeores.2007.06.007

Gudmundsson, A. (1995). Infrastructure and mechanics of volcanic systems in Iceland. *Journal of Volcanology and Geothermal Research*, *64*(1–2), 1–22. https://doi.org/10.1016/0377-0273(95)92782-q

Gudmundsson, A. (2006). How local stresses control magma-chamber ruptures, dyke injections, and eruptions in composite volcanoes. *Earth-Science Reviews*, *79*(1–2), 1–31. https://doi.org/10.1016/j.earscirev.2006.06.006

Haario, H., Laine, M., Mira, A., & Saksman, E. (2006). Dram: Efficient adaptive MCMC. *Statistics and Computing*, *16*(4), 339–354. https://doi.org/10.1007/s11222-006-9438-0

Head, M., Hickey, J., Gottsmann, J., & Fournier, N. (2019). The influence of viscoelastic crustal rheologies on volcanic ground deformation: Insights from models of pressure and volume change. *Journal of Geophysical Research: Solid Earth*, *124*(8), 8127–8146. https://doi.org/10.1029/2019jb017832

Heimisson, E. R., Hooper, A., & Sigmundsson, F. (2015). Forecasting the path of a laterally propagating dike. *Journal of Geophysical Research: Solid Earth*, *120*(12), 8774–8792. https://doi.org/10.1002/2015jb012402

Hildreth, W. (2004). Volcanological perspectives on Long Valley, Mammoth mountain, and Mono Craters: Several contiguous but discrete systems. *Journal of Volcanology and Geothermal Research*, *136*(3–4), 169–198. https://doi.org/10.1016/j.jvolgeores.2004.05.019

Hill, D. P., Pollitz, F., & Newhall, C. (2002). Earthquake–volcano interactions. *Physics Today*, *55*(11), 41–47. https://doi.org/10.1063/1.1535006

Jo, Y., Chang, C., Ji, S.-H., & Park, K.-W. (2019). In situ stress states at KURT, an underground research laboratory in South Korea for the study of high-level radioactive waste disposal. *Engineering Geology*, *259*, 105198. https://doi.org/10.1016/j.enggeo.2019.105198
Kühn, D., & Dahm, T. (2008). Numerical modelling of dyke interaction and its influence on oceanic crust formation. *Tectonophysics*, *447*(1–4), 53–65. https://doi.org/10.1016/j.tecto.2006.09.018
Laine, M. (2013). MCMC toolbox for Matlab, 2013. http://helios.fmi.fi/~lainema/mcmc
Maccaferri, F., Richter, N., & Walter, T. R. (2017). The effect of giant lateral collapses on magma pathways and the location of volcanism. *Nature Communications*, *8*(1), 1–11. https://doi.org/10.1038/s41467-017-01256-2
Maccaferri, F., Rivalta, E., Keir, D., & Acocella, V. (2014). Off-rift volcanism in rift zones determined by crustal unloading. *Nature Geoscience*, *7*(4), 297–300. https://doi.org/10.1038/ngeo2110
Maerten, F., Maerten, L., Plateaux, R., & Cornard, P. (2022). Joint inversion of tectonic stress and magma pressures using dyke trajectories (Tech. Rep.). *Copernicus Meetings*.
Mantiloni, L., Davis, T., Gaete Rojas, A. B., & Rivalta, E. (2021). Stress inversion in a gelatin box: Testing eruptive vent location forecasts with analog models. *Geophysical Research Letters*, *48*(6), e2020GL090407. https://doi.org/10.1029/2020gl090407
Mantiloni, L., Rivalta, E., Anderson, K. R., Davis, T., & Passarelli, L. (2024). InVent4Cast: Bayesian inversion of stress field and physics-based eruptive vent forecast at calderas [Software]. *GFZ*. https://doi.org/10.5880/fidgeo.2024.024
Mantiloni, L., Rivalta, E., & Davis, T. (2023a). Mechanical modeling of pre-eruptive magma propagation scenarios at calderas. *Journal of Geophysical Research: Solid Earth*, *128*(3), e2022JB025956. https://doi.org/10.1029/2022jb025956
Mantiloni, L., Rivalta, E., & Davis, T. (2023b). Sam: Simplified analytical model of dyke pathways in three dimensions [Software]. *GFZ*. https://doi.org/10.5880/GFZ.2.1.2023.001
Martel, S. J., & Muller, J. R. (2000). A two-dimensional boundary element method for calculating elastic gravitational stresses in slopes. *Pure and Applied Geophysics*, *157*(6–8), 989–1007. https://doi.org/10.1007/s000240050014
Martínez-Garzón, P., Bohnhoff, M., Kwiatek, G., & Dresen, G. (2013). Stress tensor changes related to fluid injection at the Geysers geothermal field, California. *Geophysical Research Letters*, *40*(11), 2596–2601. https://doi.org/10.1002/grl.50438
McGuire, W., & Pullen, A. (1989). Location and orientation of eruptive fissures and feederdykes at Mount Etna; influence of gravitational and regional tectonic stress regimes. *Journal of Volcanology and Geothermal Research*, *38*(3–4), 325–344. https://doi.org/10.1016/0377-0273(89)90046-2
McLeod, P., & Tait, S. (1999). The growth of dykes from magma chambers. *Journal of Volcanology and Geothermal Research*, *92*(3–4), 231–245. https://doi.org/10.1016/s0377-0273(99)00053-0
McTigue, D. F., & Mei, C. C. (1987). Gravity-induced stresses near axisymmetric topography of small slope. *International Journal for Numerical and Analytical Methods in Geomechanics*, *11*(3), 257–268. https://doi.org/10.1002/nag.1610110304
Muirhead, J. D., Van Eaton, A. R., Re, G., White, J. D., & Ort, M. H. (2016). Monogenetic volcanoes fed by interconnected dikes and sills in the Hopi Buttes volcanic field, Navajo Nation, USA. *Bulletin of Volcanology*, *78*(2), 1–16. https://doi.org/10.1007/s00445-016-1005-8
Muller, J. R., Ito, G., & Martel, S. J. (2001). Effects of volcano loading on dike propagation in an elastic half-space. *Journal of Geophysical Research*, *106*(B6), 11101–11113. https://doi.org/10.1029/2000JB900461
Muller, O. H., & Pollard, D. D. (1977). The stress state near Spanish Peaks, Colorado determined from a dike pattern. *Pure and Applied Geophysics*, *115*(1–2), 69–86. https://doi.org/10.1007/bf01637098
Neri, M., Rivalta, E., Maccaferri, F., Acocella, V., & Cirrincione, R. (2018). Etnean and Hyblean volcanism shifted away from the Malta Escarpment by crustal stresses. *Earth and Planetary Science Letters*, *486*, 15–22. https://doi.org/10.1016/j.epsl.2018.01.006
Nielsen, G., Maack, R., Gudmundsson, A., & Gunnarsson, G. I. (2000). Completion of Krafla geothermal power plant. In *Proc. world geothermal congress* (pp. 3259–3264).
Nikkhoo, M., & Walter, T. R. (2015). Triangular dislocation: An analytical, artefact-free solution. *Geophysical Journal International*, *201*(2), 1119–1141. https://doi.org/10.1093/gji/ggv035
Orsi, G., De Vita, S., & Di Vito, M. (1996). The restless, resurgent Campi Flegrei nested caldera (Italy): Constraints on its evolution and configuration. *Journal of Volcanology and Geothermal Research*, *74*(3–4), 179–214. https://doi.org/10.1016/s0377-0273(96)00063-7
Pansino, S., & Taisne, B. (2019). How magmatic storage regions attract and repel propagating dikes. *Journal of Geophysical Research: Solid Earth*, *124*(1), 274–290. https://doi.org/10.1029/2018jb016311
Persson, P.-O., & Strang, G. (2004). A simple mesh generator in MATLAB. *SIAM Review*, *46*(2), 329–345. https://doi.org/10.1137/s0036144503429121
Pinel, V., & Jaupart, C. (2004). Magma storage and horizontal dyke injection beneath a volcanic edifice. *Earth and Planetary Science Letters*, *221*(1–4), 245–262. https://doi.org/10.1016/s0012-821x(04)00076-7
Pollard, D. D. (1987). Elementary fracture mechanics applied to the structural interpretation of dykes. *Mafic Dyke Swarms*, *34*, 5–24.
Rabbath, C., & Corriveau, D. (2019). A comparison of piecewise cubic Hermite interpolating polynomials, cubic splines and piecewise linear functions for the approximation of projectile aerodynamics. *Defence Technology*, *15*(5), 741–757. https://doi.org/10.1016/j.dt.2019.07.016
Reches, Z., & Fink, J. (1988). The mechanism of intrusion of the Inyo dike, Long Valley Caldera, California. *Journal of Geophysical Research*, *93*(B5), 4321–4334. https://doi.org/10.1029/jb093ib05p04321
Rinaldi, A. P., Todesco, M., & Bonafede, M. (2010). Hydrothermal instability and ground displacement at the Campi Flegrei caldera. *Physics of the Earth and Planetary Interiors*, *178*(3–4), 155–161. https://doi.org/10.1016/j.pepi.2009.09.005
Rivalta, E., Corbi, F., Passarelli, L., Acocella, V., Davis, T., & Di Vito, M. A. (2019). Stress inversions to forecast magma pathways and eruptive vent location. *Science Advances*, *5*(7), eaau9784. https://doi.org/10.1126/sciadv.aau9784
Roman, A., & Jaupart, C. (2014). The impact of a volcanic edifice on intrusive and eruptive activity. *Earth and Planetary Science Letters*, *408*, 1–8. https://doi.org/10.1016/j.epsl.2014.09.016
Savage, W. Z., Swolfs, H. S., & Amadei, B. (1992). On the state of stress in the near-surface of the Earth's crust. *Pure and Applied Geophysics*, *138*(2), 207–228. https://doi.org/10.1007/bf00878896
Selva, J., Orsi, G., Di Vito, M. A., Marzocchi, W., & Sandri, L. (2012). Probability hazard map for future vent opening at the Campi Flegrei caldera, Italy. *Bulletin of Volcanology*, *74*(2), 497–510. https://doi.org/10.1007/s00445-011-0528-2
Seropian, G., Kennedy, B. M., Walter, T. R., Ichihara, M., & Jolly, A. D. (2021). A review framework of how earthquakes trigger volcanic eruptions. *Nature Communications*, *12*(1), 1004. https://doi.org/10.1038/s41467-021-21166-8
Sigmundsson, F., Hooper, A., Hreinsdóttir, S., Vogfjörd, K. S., Ófeigsson, B. G., Heimisson, E. R., et al. (2015). Segmented lateral dyke growth in a rifting event at Bárdarbunga volcanic system, Iceland. *Nature*, *517*(7533), 191–195. https://doi.org/10.1038/nature14111
Silverman, B. W. (1986). *Density estimation for statistics and data analysis* (Vol. 26). CRC press.

Slim, M., Perron, J. T., Martel, S. J., & Singha, K. (2015). Topographic stress and rock fracture: A two-dimensional numerical model for arbitrary topography and preliminary comparison with borehole observations. *Earth Surface Processes and Landforms*, *40*(4), 512–529. https://doi.org/10.1002/esp.3646

Tarantola, A. (2005). *Inverse problem theory and methods for model parameter estimation*. SIAM.

Walter, T. R., Troll, V. R., Cailleau, B., Belousov, A., Schmincke, H.-U., Amelung, F., & Bogaard, P. V. D. (2005). Rift zone reorganization through flank instability in ocean island volcanoes: An example from Tenerife, canary Islands. *Bulletin of Volcanology*, *67*(4), 281–291. https://doi.org/10.1007/s00445-004-0352-z

Wiprut, D., & Zoback, M. (2000). Constraining the stress tensor in the Visund field, Norwegian North Sea: Application to wellbore stability and sand production. *International Journal of Rock Mechanics and Mining Sciences*, *37*(1–2), 317–336. https://doi.org/10.1016/s1365-1609(99)00109-4

Xu, W., Rivalta, E., & Li, X. (2017). Magmatic architecture within a rift segment: Articulate axial magma storage at Erta Ale volcano, Ethiopia. *Earth and Planetary Science Letters*, *476*, 79–86. https://doi.org/10.1016/j.epsl.2017.07.051

Zhan, Y., Roman, D. C., Le Mével, H., & Power, J. A. (2022). Earthquakes indicated stress field change during the 2006 unrest of Augustine Volcano, Alaska. *Geophysical Research Letters*, *49*(10), e2022GL097958. https://doi.org/10.1029/2022gl097958